Chinese Journal of Structural Chemistry 45 (2026) 100764

Contents lists available at ScienceDirect

Chinese Journal of Structural Chemistry

journal homepage: www.journals.elsevier.com/chinese-journal-of-structural-chemistry

Article

Chiral Ln_3Co_5 clusters with geometry-dependent chiroptical and magneto-optical properties

Ya-Xuan Xue[a], Han Xu[a], Jia-Nan Chen[a], Hai-Quan Tian[b], Tao Jia[a], Wei-Dong Liu[a], Chong-Yang Li[a], La-Sheng Long[a], Lan-Sun Zheng[a], Xiang-Jian Kong[a,*]

[a] State Key Laboratory of Physical Chemistry of Solid Surfaces, Department of Chemistry, College of Chemistry and Chemical Engineering, Xiamen University, Xiamen, 361005, China
[b] Shandong Provincial Key Laboratory of Chemical Energy Storage and Novel Cell Technology, School of Chemistry and Chemical Engineering, Liaocheng University, Liaocheng, 252059, China

ARTICLE INFO

Keywords:
Circular dichroism
Magnetic circular dichroism
Ligand field
Chiroptical behavior

ABSTRACT

Heterometallic 3d-4f clusters represent a promising class of multifunctional molecular materials, driven by the synergistic interactions between d- and f-electrons. Incorporating chirality into these systems further expands their potential applications, particularly in chiroptical and magneto-optical technologies. Herein, we report the successful synthesis of chiral [Ln_3Co_5] (Ln = Er and Y) clusters using binaphthol-based ligands. Single-crystal X-ray diffraction reveals the coexistence of two distinct Co^{2+} coordination geometries: six-coordinate octahedron and five-coordinate trigonal bipyramid. Spectroscopic analyses demonstrate geometry-dependent chiroptical behavior: pentacoordinate Co^{2+} ions predominantly contribute to the circular dichroism (CD) features, while both geometries exhibit distinguishable signals in the magnetic circular dichroism (MCD) spectra. Notably, a pronounced magnetic dipole transition ($^4I_{15/2} \rightarrow {}^4I_{13/2}$) from Er^{3+} centers is observed in the near-infrared MCD region, displaying a high g-factor of 0.0078 T^{-1}. This work highlights the configuration- and ligand field-dependent chiroptical responses in 3d-4f systems, providing new insights for the rational design of advanced magneto-optical devices.

1. Introduction

Heterometallic 3d-4f clusters offer a unique electronic platform for constructing multifunctional molecular-based materials, owing to the synergistic interactions between d- and f-electrons. These systems have demonstrated remarkable performance in areas such as single-molecule magnets (SMMs), chiral catalysis, and magneto-optical devices [1–6]. The incorporation of chirality into 3d-4f clusters further enhances their functional potential and has become a frontier research field in the design of advanced materials [7–9]. Notably, chiral 3d-4f clusters serve as model systems for exploring the magnetochiral dichroism (MChD) effect [10,11], which has potential applications in magneto-optical data storage, optoelectronics, and spintronics [12].

Among 3d-block metal ions, Co^{2+} is notable for its diverse coordination geometries—such as octahedral, tetrahedral, trigonal bipyramidal and square planar—stemming from its electronically versatile d^7 configuration, which supports both high-spin and low-spin states depending on the ligand field strength. Heterometallic 3d-4f clusters incorporating Co^{2+} have shown wide applicability in SMMs and magneto-optical materials [13,14]. However, the diverse coordination geometries of Co^{2+} present analytical challenges. When multiple coordination geometries coexist—especially in systems probed by near-infrared spectroscopy—they complicate spectral interpretation.

In this study, we successfully synthesized chiral [Ln_3Co_5] clusters using chiral binaphthol ligands, with the molecular formula $[Ln_3Co_5(R/S\text{-}L)_6(Ac)_4(CH_3CN)_2(CH_3OH)_7(\mu_4\text{-}O)(H_2O)_3]\cdot(Ac)\cdot(H_2O)_{12}$ (**Ln_3Co_5**, Ln = Er and Y, L = $C_{20}H_{12}O_2{}^{2-}$). Single-crystal X-ray diffraction analysis revealed that each cluster features two distinct Co^{2+} coordination geometries: a six-coordinate octahedral geometry and a five-coordinate trigonal bipyramidal geometry. Comprehensive spectroscopic characterization enabled the clear assignment of electronic transitions associated with each geometry. Notably, this work establishes a robust framework for analyzing spectral signatures of multiple Co^{2+} coordination geometries within a single cluster. These findings provide critical insights for the design of chiral molecular devices with enhanced magneto-optical coupling and tunable spectroscopic properties,

This article is part of a special issue entitled: Structural Chemistry published in Chinese Journal of Structural Chemistry.

* Corresponding author. Collaborative Innovation Center of Chemistry for Energy Materials, China.
E-mail address: xjkong@xmu.edu.cn (X.-J. Kong).

https://doi.org/10.1016/j.cjsc.2025.100764
Received 1 August 2025; Received in revised form 24 September 2025; Accepted 6 October 2025
Available online 11 October 2025

advancing the site-specific coordination engineering of functional molecular materials.

2. Results and discussion

2.1. Single-crystal structures

Single-crystal X-ray diffraction analysis reveals that the cluster crystallizes in the chiral orthorhombic space group $P2_12_12_1$, belonging to the D_2 point group. Detailed crystallographic data are presented in Table S1–10. The structure comprises a central +1-charged metal cluster stabilized by peripheral acetate ion and solvent molecules. Powder X-ray diffraction (PXRD, Fig. S1) analysis confirms the phase purity of the samples. X-ray photoelectron spectroscopy (XPS, Fig. S2) and bond valance sum calculations (Table S11) demonstrate that all Co ions adopt the high-spin Co^{2+} oxidation state. The structures of ***R/S*–Er$_3$Co$_5$** (Fig. 1(b)) and ***R/S*–Y$_3$Co$_5$** (Fig. S5) have been confirmed to be isostructural by single-crystal X-ray diffraction analysis. Here, we present a detailed structural analysis of ***R/S*–Er$_3$Co$_5$** as a representative example. As shown in Fig. 1, the [Er_3Co_5] cluster is constructed from six chiral binaphthol (BINOL) ligands, three acetate ions, and a central μ_4-oxo bridge that links three Er^{3+} and five Co^{2+} ions. The core structure features a trigonal bipyramidal geometry formed with three Er^{3+} ions occupying the equatorial positions and two Co^{2+} ions at the axial positions, all bridged by the central μ_4-oxo group. Three peripheral Co^{2+} ions are connected to the Er^{3+} centers through the chiral BINOL ligands and acetate bridges, completing the intricate cluster architecture. The stability of the cluster structure was verified by high-resolution electrospray ionization mass spectrometry (HR-ESI-MS) spectra, as shown in Fig. 1(d) and Fig. S3. Fig. 1(d) displays the experimental values and theoretical fitting of +2 charged species signals for the ***S*–Er$_3$Co$_5$** cluster. Three intense main peaks at $m/z = 1459.06$ (c), 1480.07 (d), and 1500.58 (e) correspond to $[Er_3Co_5(L)_6(Ac)_3(CH_3CN)(CH_3OH)_4(H_2O)_3(O)]^{2+}$ (calcd. 1459.08, L = $C_{20}H_{12}O_2^{2-}$), $[Er_3Co_5(L)_6(Ac)_3(CH_3CN)(CH_3OH)_7(O)]^{2+}$ (calcd. 1480.10), and $[Er_3Co_5(L)_6(Ac)_3(CH_3CN)_2(CH_3OH)_7(O)]^{2+}$ (calcd. 1500.61), respectively.

Steric hindrance effects induce distinct coordination environments among the metal centers. Two Er^{3+} ions adopt seven-coordinate geometries, while the third Er^{3+} ion is six-coordinated (Fig. S4). The five Co^{2+} ions exhibit two clearly differentiated coordination modes: (i) Core Co^{2+} adopts a five-coordinate trigonal bipyramidal geometry that partially distorts toward tetrahedral symmetry. This distortion manifests in O(axial)−Co−O(equatorial) bond angles below 90° and elongated Co–O (axial) bond distances, indicative of a structural tendency approaching C_{3v} symmetry (Fig. S4). (ii) Peripheral Co^{2+} displays a six-coordinate

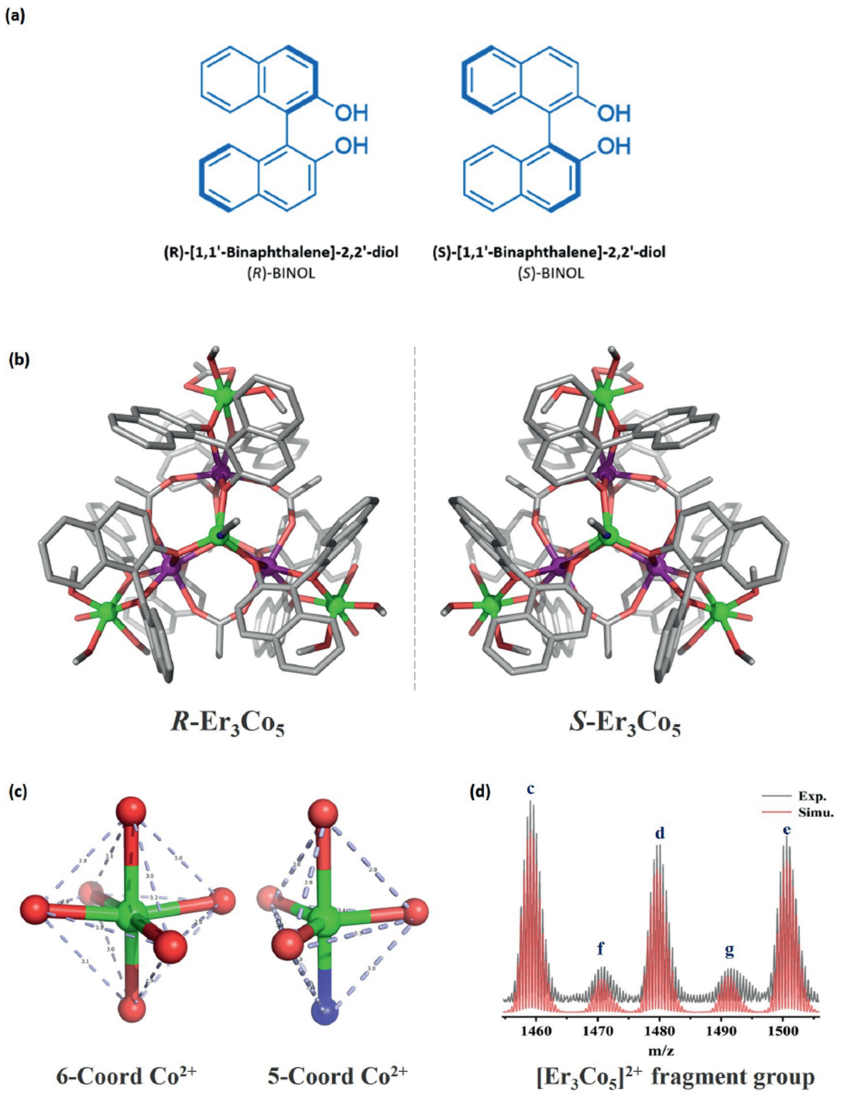

Fig. 1. (a) Schematic structure of chiral binaphthol ligand. (b) Schematic representation of the enantiomeric ***R/S*–Er$_3$Co$_5$** cluster structure; (c) Coordination modes of Co^{2+} centers, showing the six-coordinate octahedral geometry (left) and five-coordinate trigonal bipyramidal geometry (right); (d) Experimental and simulated HR-ESI-MS spectra of the $[Er_3Co_5]^{2+}$ fragment group in the ***S*–Er$_3$Co$_5$** cluster. Color code: Purple, Er^{3+}; green, Co^{2+}; gray, C; red, O; blue, N.

octahedral geometry with slight distortions from ideal O_h symmetry. Continuous shape measures (CShM) analysis indicates limited deviations for both coordination geometries, allowing approximate treatment under D_{3h} (trigonal bipyramid) and O_h (octahedron) symmetry frameworks (Table S12–13) [33,43]. Furthermore, CShM analysis was performed for the Ln^{3+} ions in the cluster structures, with the results detailed in Table S14–15. These distinct Co^{2+} coordination modes directly influence their respective spectroscopic signatures, as discussed in the following spectroscopic analysis section.

2.2. Magneto-optical properties

To investigate the chiroptical properties of the synthesized cluster compounds, solutions of ***R/S*–Er$_3$Co$_5$** and ***R/S*–Y$_3$Co$_5$** were prepared in DMF at varying concentrations (10, 15, and 20 g/L) and analyzed using a JASCO-1700 circular dichroism (CD) spectrometer (Fig. 2). Comparative analysis of the CD spectra, in combination with ligand field theory (LFT), enabled assignment of characteristic absorption bands associated with Co^{2+} d-d transitions. According to LFT, the ligand field splitting energy (Δ) correlates positively with the energy of d-d transitions and varies depending on the coordination geometry. For Co^{2+}, the ligand field splitting energy in an octahedral environment (Δ_{oct}) is substantially greater than that in a trigonal bipyramidal (Δ_{TBP}) geometry. CD spectroscopy reveals that five-coordinate Co^{2+} centers exhibit stronger Cotton effects than their six-coordinate counterparts [15,48].

The assignment of absorption bands was further supported by Tanabe-Sugano diagrams and LFT: The band near 480 nm corresponds to the $^4A_2' \rightarrow {}^4E''(P)$ transition of five-coordinate Co^{2+}. The intense peak at 567 nm arises from the $^4A_2' \rightarrow {}^4A_2'(P)$ transition of five-coordinate Co^{2+}, accompanied by a shoulder peak at ~591 nm. Broad absorption features observed between 710 and 1090 nm (maximum at 935 nm) and 1090–1695 nm range (maximum at 1296 nm) are attributed to $^4A_2' \rightarrow {}^4E'$ and $^4A_2' \rightarrow {}^4E''$ transitions of five-coordinate Co^{2+}, respectively [18–21, 34]. Notably, the latter region may overlap with the spin-allowed $^4T_{1g} \rightarrow {}^4T_{2g}$ transition of six-coordinate Co^{2+}, resulting in non-Gaussian line shapes [15–21]. For high-spin Co^{2+}, the absorption bands in the 500–650 nm region are inherently associated with the $^4T_{1g} \rightarrow {}^4T_{1g}$ (P) transition of six-coordinate Co^{2+} ions, which are more clearly resolved in MCD spectra [16,17,22,23]. Although CD spectroscopy typically exhibits limited sensitivity to parity-forbidden f-f transitions of lanthanide ions due to their weak magnetic dipole character, weak yet distinct Er^{3+}-derived signals were resolvable in ***R/S*–Er$_3$Co$_5$** clusters. A prominent sharp peak at 515 nm is assigned to the hypersensitive $^4I_{15/2} \rightarrow {}^2H_{11/2}$ electric dipole transition of Er^{3+}. Furthermore, a broad magnetic dipole transition spanning 1496–1581 nm corresponds to the $^4I_{15/2} \rightarrow {}^4I_{13/2}$ transition [26,27,38–42].

Magnetic circular dichroism (MCD) measurements were performed at room temperature under an external magnetic field of 1.6 T with alternating NS (north-south) and SN (south-north) directions to investigate the magneto-optical properties of the ***R/S*–Ln$_3$Co$_5$** clusters. As illustrated in Fig. 3, the MCD spectra were calculated using the formula [24,25]:

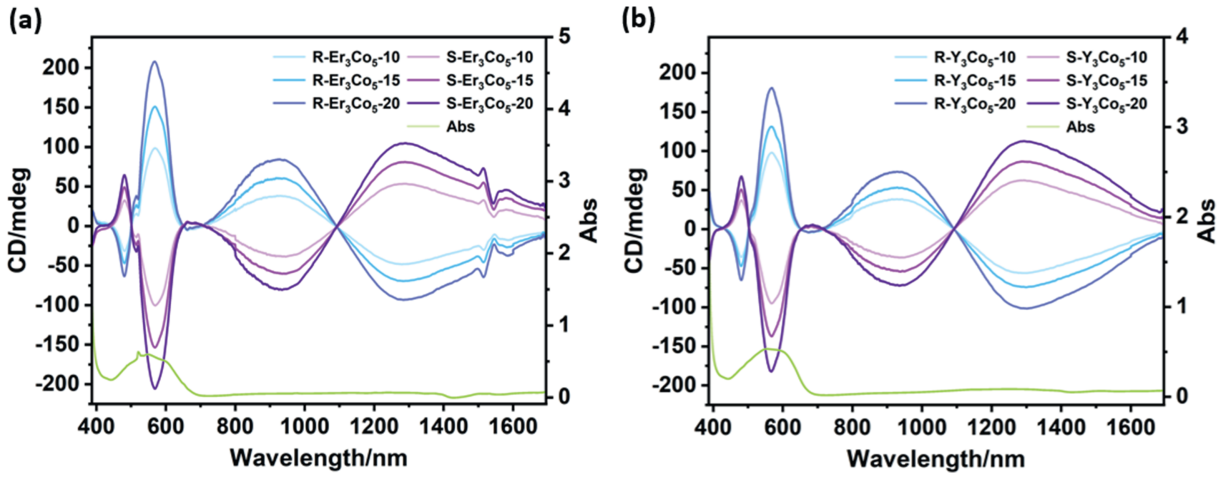

Fig. 2. CD spectra of ***R/S*–Er$_3$Co$_5$** (a) and ***R/S*–Y$_3$Co$_5$** (b) clusters at different concentrations (10, 15, 20 g/L) and the green line in the figure represents the absorption spectrum.

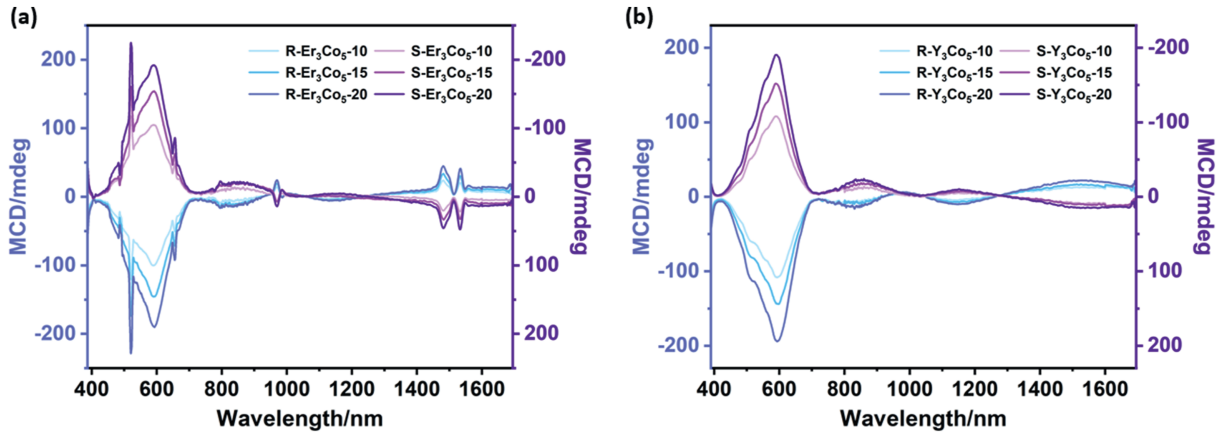

Fig. 3. MCD spectra of ***R/S*–Er$_3$Co$_5$** (a) and ***R/S*–Y$_3$Co$_5$** (b) clusters at different concentrations (10, 15, 20 g/L).

$$MCD = (CD(NS) - CD(SN))/2 \quad (1)$$

At room temperature, the CD spectra are dominated by d-d transitions of five-coordinate Co^{2+} [15,48]. The MCD spectra revealed distinct magneto-optical contributions from both five- and six-coordinate Co^{2+} centers. The five-coordinate Co^{2+} centers in D_{3h} symmetry exhibit strong magnetic anisotropy due to crystal field splitting of the excited state, generating A-term MCD signals via Zeeman splitting. It should be noted that in systems with degenerate ground states, Zeeman splitting of the ground state can concurrently contribute to C-term signals, particularly at low temperatures. However, for the trigonal bipyramidal Co^{2+} center with a non-degenerate ground state ($^4A_2'$), C-term contributions are absent [20,50]. In contrast, the octahedral six-coordinate Co^{2+} ions showed coexisting A- and C-term MCD contributions. For the octahedral Co^{2+} centers, A-term signals originated from magnetic-field-induced splitting of degenerate excited states (e.g., $^4T_{1g} \rightarrow {}^4T_{2g}$ transitions), while C-term contributions arise from ground-state splitting under the applied magnetic field [49,50]. In the analysis of variable-temperature magnetization curves (Fig. 4), the $\chi_m T$ (T) behavior and Curie-Weiss parameters suggest ground-state splitting, tentatively supporting C-term dominance. This assignment, however, requires further confirmation through variable-temperature MCD studies to unequivocally exclude B-term contributions. This dual behavior highlights the interplay between ligand-field symmetry (A-term dominance in low-symmetry sites) and spin-orbit interactions (C-term emergence in high-symmetry sites), providing critical insights into the magneto-structural correlations within mixed-coordination clusters [35–37].

LFT analysis, supported by Tanabe-Sugano diagrams for D_{3h} (trigonal bipyramidal) and O_h (octahedral) symmetries, confirmed that the ligand field splitting energy (Δ) for octahedral Co^{2+} is weaker than that of trigonal bipyramidal Co^{2+}, particularly in systems coordinated by weak-field ligands. To isolate the Co^{2+}-based contributions from overlapping rare-earth ion transitions, the MCD spectra of ***R/S*–Y_3Co_5** clusters (Fig. 3(b)) were analyzed. Combined with the absorption spectra of the cluster samples (Fig. S6), the assignments for five-coordinate Co^{2+} (D_{3h}) included transitions at 471 nm ($^4A_2' \rightarrow {}^4E''(P)$), 555–621 nm ($^4A_2' \rightarrow {}^4A_2'(P)$), 840 nm ($^4A_2' \rightarrow {}^4E'$), and 1277–1695 nm ($^4A_2' \rightarrow {}^4E''$, peak at 1520 nm) [15,18–21]. The characteristic peaks of six-coordinate cobalt ions partially overlap with those of five-coordinate cobalt ions. For six-coordinate Co^{2+} (O_h), transitions were identified at 462 nm ($^4T_{1g} \rightarrow {}^2T_{1g}(H)$) and 472–685 nm ($^4T_{1g} \rightarrow {}^4T_{1g}(P)$). The transitions at 1067–1275 nm and 1277–1695 nm were identified $^4T_{1g} \rightarrow {}^4T_{2g}$ of six-coordinate Co^{2+} [16,17,22,23]. The splitting of transitions in six-coordinate cobalt ions is caused by the Jahn-Teller effect. The transition analysis of six-coordinate Co^{2+} ions incorporated MCD spectroscopy data of $Co(Ac)_2$ (Fig. S7). In addition to Co^{2+} transitions, the MCD spectra also revealed clearly resolved f-f transitions associated with Er^{3+} ions. Assignments included weakly resolved transitions at 412–486 nm ($^4I_{15/2} \rightarrow {}^4F_{3/2}/{}^4F_{5/2}$), a sharp hypersensitive transition at 520 nm ($^4I_{15/2} \rightarrow {}^2H_{11/2}$, $\Delta J = 2$, $\Delta L = 1$, $\Delta S = 1$), and distinct peaks at 655 nm ($^4I_{15/2} \rightarrow {}^4F_{9/2}$, $\Delta J = 3$, $\Delta L = 3$, $\Delta S = 0$), 797 nm ($^4I_{15/2} \rightarrow {}^4I_{9/2}$, $\Delta J = 3$, $\Delta L = 0$, $\Delta S = 0$), and 969 nm ($^4I_{15/2} \rightarrow {}^4I_{11/2}$, $\Delta J = 2$, $\Delta L = 0$, $\Delta S = 0$). Magnetic dipole transitions dominated the near-infrared region, with peaks at 1484 and 1535 nm assigned to $^4I_{15/2} \rightarrow {}^4I_{13/2}$ ($\Delta J = 1$, $\Delta L = 0$, $\Delta S = 0$) [26–28,38–42]. These observations confirm the simultaneous presence and spectroscopic resolution of both transition metal and lanthanide centers within the heterometallic cluster environment.

The magneto-optical g-factor was calculated using the formula:

$$g(\lambda) = \frac{\varepsilon_+ - \varepsilon_-}{\varepsilon \times B(T)} = \frac{\Delta\varepsilon_{MCD}(\lambda)}{\varepsilon(\lambda)}\left(T^{-1}\right) \quad (2)$$

where ε_+ and ε_- represent the extinction coefficients for right and left circularly polarized light, respectively, ε is the average extinction coefficient, and B is the magnetic field strength (in tesla) [29,30]. To avoid spectral overlap between rare-earth and transition metal transitions, the g-values for Er^{3+} and Co^{2+} were derived from the MCD spectra of ***R/S*–Er_3Co_5** and ***R/S*–Y_3Co_5** clusters, respectively (Table S16 and S17). Magneto-optical anisotropy analysis revealed distinct behaviors for Er^{3+} and Co^{2+} ions. For Er^{3+}, the largest g-value of 0.0078 T^{-1} was observed at 1481.2 nm, corresponding to the magnetic dipole transition $^4I_{15/2} \rightarrow {}^4I_{13/2}$, with an additional g-value of 0.0064 T^{-1} recorded at 656.2 nm. In contrast, for the Co^{2+} centers, a maximum g-factor of 0.0058 T^{-1} was recorded at 834.8 nm.

The magnitude of the g-value further reflects the distinct responses of rare earth metals and transition metals to an external magnetic field. For rare-earth ions, the peak position of the maximum g-value aligns with transitions that possess strong magnetic dipole character, reinforcing their pivotal role in generating pronounced MCD signals. We observed a slight discrepancy between the peak position of the highest-intensity feature in the MCD spectrum and the peak position of the maximum g-value signal. This difference arises because the MCD peak position is associated with the direct transition energy between the ground and excited states, corresponding to the wavelength where spectral absorption differences are maximized. In contrast, the g-factor peak position relates to the asymmetry of magnetic-field-induced energy level splitting, with its extremum occurring at the location of energy-level crossing or the strongest magnetic moment coupling—rather than at the energy difference (ΔE) between states.

2.3. Magnetic properties

The enantiomeric R/S forms of both clusters exhibited magnetically equivalent behavior; thus, the R-enantiomer clusters were selected as representative models for variable-temperature (Fig. 4) and variable-

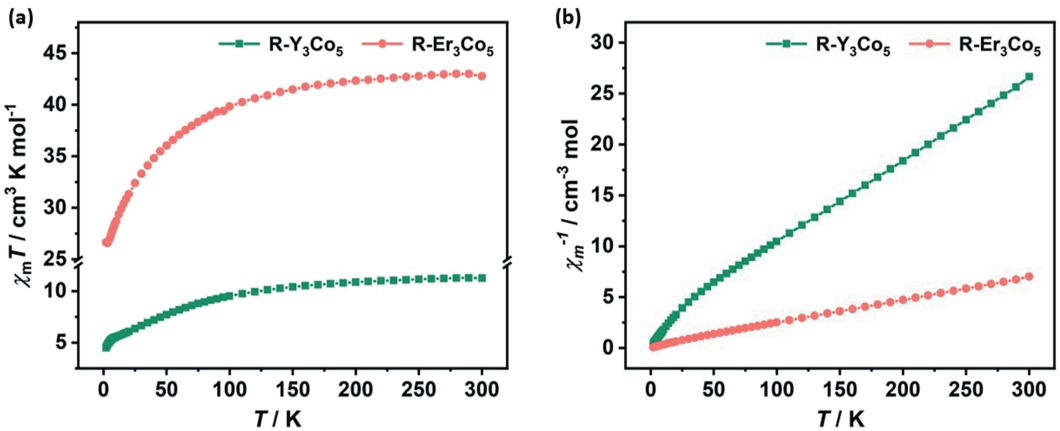

Fig. 4. Temperature-dependent magnetization curves of ***R*–Y_3Co_5** and ***R*–Er_3Co_5** measured under 1000 Oe (2–300 K).

field (Fig. S8) magnetic studies. For cluster ***R*–Er$_3$Co$_5$**, temperature-dependent molar magnetic susceptibility ($\chi_m T$) measurements were carried out under an applied field of 1000 Oe (Fig. 4(a)). At 300 K, the observed $\chi_m T$ value of 42.78 cm^3 K mol^{-1} closely matched the theoretical value of 43.82 cm^3 K mol^{-1} for three Er^{3+} ($J = 15/2$, $g_J = 6/5$) and five Co^{2+} ($S = 3/2$, $g = 2.2$) [44–47], confirming paramagnetic nature of the complex in the high-temperature regime. Upon cooling, $\chi_m T$ gradually decreased, reaching 26.57 cm^3 K mol^{-1} at 4 K, consistent with antiferromagnetic interactions. This trend in the temperature range of 100–300 K was rationalized by Curie-Weiss fitting (C = 44.9 cm^3 K mol^{-1}, $\theta = -12.62$ K) (Fig. 4(b)), suggesting weak antiferromagnetic exchange mediated via Er–O–Co bridging pathways [31,32].

Cluster ***R*–Y$_3$Co$_5$** (Fig. 4(a)) exhibited distinct Co^{2+}-centered magnetic behavior, as the Y^{3+} ions ([Kr]4d^0, diamagnetic) contribute no magnetic moment. The $\chi_m T$ value at 300 K (11.25 cm^3 K mol^{-1}) is consistent with the theoretical value expected for five high-spin Co^{2+} ions ($S = 3/2$, $g = 2.2$). Curie-Weiss fitting over the 100–300 K range (C = 12.54 cm^3 K mol^{-1}, $\theta = -31.5$ K) indicates strong exchange interactions. Upon cooling, $\chi_m T$ decreased gradually down to 9 K, followed by a sharper drop to 4.49 cm^3 K mol^{-1} at 2 K. This behavior contrasts with ***R*–Er$_3$Co$_5$**, demonstrating stronger Co–Co superexchange compared to the lanthanide-mediated interactions [31]. The contrasting magnetic responses directly correlate with electronic configurations. Er^{3+}'s 4f electrons (shielded by 5s^{2}5p^6 orbitals) generate high para-magnetism (μ_{eff} = 9.6 μB) but inefficient superexchange, while transition metal systems achieve enhanced coupling through direct d-orbital interactions. These insights underline the importance of electronic configuration in tailoring magnetic interactions within 3d-4f heterometallic assemblies.

3. Conclusion

In summary, we successfully synthesized two pairs of chiral ***R*/*S*–Ln$_3$Co$_5$** (Ln = Er, Y) clusters using a chiral binaphthol-based ligand. The cluster framework features two distinct coordination environments for Co^{2+} ions—hexacoordinate (octahedral) and pentacoordinate (trigonal bipyramidal)—each contributing differently to the observed chiroptical properties. In the CD spectra, signals from pentacoordinate Co^{2+} ions dominate, while MCD spectra exhibit clear contributions from both coordination types. Importantly, the MCD analysis of the Er-containing cluster reveals a pronounced magnetic dipole transition in the near-infrared region ($^4I_{15/2} \rightarrow {}^4I_{13/2}$) with a high g-value of 0.0078 T^{-1}, underscoring the sensitivity of rare-earth magnetic dipole transitions to MCD effects. These results suggest that such clusters are promising candidates for future exploration of MChD. Beyond their magneto-chiroptical functionality, these heterometallic clusters offer valuable insights into structure-property relationships in systems with mixed coordination geometries. The findings offer the reference for the rational design of molecular magneto-optical material.

4. Experimental

4.1. Physical measurements

The crystallographic data were collected on a Rigaku Oxford diffraction XtaLAB synergy diffractometer with micro-focus sealed X-ray Cu Kα radiation (λ = 1.54184 Å) at 100 K. The CD spectra were recorded on a JASCO J-1700 at room temperature. The MCD spectra were measured on the JASCO J-1700 equipped with a JASCO PM-491 compact permanent magnet (1.6 T). The absorption spectra were measured by a Cary-1500 UV-vis-NIR spectrometer. Microanalyses of C, H and N elements were carried out with an element analyzer (EA, Flash Smart CHNS). The PXRD studies were performed using a Rigaku Ultima-IV diffractometer with Cu-Kα radiation (25.0 kV, 100.0 mA). The HR-ESI-MS of samples was performed on Agilent Technologies ESI-TOF-MS 6224A instrumentation. The XPS was measured on the Thermo Scientific ESCALAB Xi+. Magnetic measurements were carried out with a Quantum Design MPMS-SQUID magnetometer working in the 2–300 K range.

4.2. Synthesis

Preparation of $[Er_3Co_5(R/S\text{-}L)_6(Ac)_4(CH_3CN)_2(CH_3OH)_7(\mu_4\text{-}O)(H_2O)_3]\cdot(Ac)\cdot(H_2O)_{12}$ (L = $C_{20}H_{12}O_2^{2-}$)

Er(Ac)$_3$·4H$_2$O (0.1 mmol) was charged into a 25 mL Schlenk reactor and dissolved in methanol (6 mL). A pre-prepared solution of $Co(ClO_4)_2\cdot 6H_2O$ (0.3 mmol, 0.5 M) and another solution of *R*-(−)-1,1′-bi-2-naphthol (*R*-BINOL, 0.3 mmol, 0.5 M) were sequentially injected via syringe into the reaction mixture, followed by the dropwise addition of triethylamine (0.3 mmol). After stirring at room temperature for 15 min, it was placed in an oven at 80 °C for the reaction. Following 72 h, abundant peach-red lamellar crystals of ***R*–Er$_3$Co$_5$** were observed adhering to both the flask walls and bottom with the yield of 29.1% (based on erbium(III) acetate tetrahydrate). Anal. Calcd. for $Er_3Co_5C_{141}H_{151}N_2O_{45}$ (FW = 3390.14): C, 49.95%; H, 4.49%; N, 0.83%. Found: C,49.56%; H, 4.22 %; N, 0.81%.

The synthetic procedure for ***S*–Er$_3$Co$_5$** is identical to that of ***R*–Er$_3$Co$_5$** except that *R*-BINOL is replaced by *S*-BINOL in 28.7% yield (based on erbium(III) acetate tetrahydrate). Anal. Calcd. for $Er_3Co_5C_{141}H_{151}N_2O_{45}$ (FW = 3390.14): C, 49.95%; H, 4.49%; N, 0.83%. Found: C,49.33%; H, 4.17%; N, 0.82%.

Preparation of $[Y_3Co_5(R/S\text{-}L)_6(Ac)_4(CH_3CN)_2(CH_3OH)_7(\mu_4\text{-}O)(H_2O)_3]\cdot(Ac)\cdot(H_2O)_{12}$ (L = $C_{20}H_{12}O_2^{2-}$)

Y(Ac)$_3$·xH$_2$O (0.1 mmol) was charged into a 25 mL Schlenk reactor and dissolved in methanol (6 mL). A pre-prepared solution of $Co(ClO_4)_2\cdot 6H_2O$ (0.3 mmol, 0.5 M) and a solution of *R*-(−)-1,1′-bi-2-naphthol (*R*-BINOL, 0.3 mmol, 0.5 M) were sequentially injected via syringe into the reaction mixture. The system was magnetically stirred at room temperature for 5 min, followed by the dropwise addition of triethylamine (0.3 mmol). Stirring was continued at room temperature for 15 min, after which the reaction mixture was transferred to an oven set at 80 °C to proceed with the reaction. Following a 72 h reaction period, abundant peach-red lamellar crystals of ***R*–Y$_3$Co$_5$** were observed adhering to both the inner walls and the bottom of the flask, with a yield of 31% (based on yttrium acetate hydrate). Anal. Calcd. for $Y_3Co_5C_{141}H_{151}N_2O_{45}$ (FW = 3155.08): C, 53.68%; H, 4.82%; N, 0.89%. Found: C, 53.26%; H, 4.50%; N, 0.87%.

The synthetic procedure for ***S*–Y$_3$Co$_5$** is identical to ***R*–Y$_3$Co$_5$** except the replacement of *R*-BINOL by *S*-BINOL with the yield of 30.5% (based on yttrium acetate hydrate). Anal. Calcd. for $Y_3Co_5C_{141}H_{151}N_2O_{45}$ (FW = 3155.08): C, 53.68%; H, 4.82%; N, 0.89%. Found: C, 53.55%; H, 4.56%; N, 0.88%.

CRediT authorship contribution statement

Ya-Xuan Xue: Writing – original draft, Validation, Methodology, Investigation, Formal analysis, Data curation. **Han Xu:** Methodology, Investigation, Formal analysis, Data curation. **Jia-Nan Chen:** Investigation, Formal analysis, Data curation. **Hai-Quan Tian:** Formal analysis, Data curation. **Tao Jia:** Investigation, Formal analysis, Data curation. **Wei-Dong Liu:** Investigation, Formal analysis, Data curation. **Chong-Yang Li:** Investigation, Formal analysis. **La-Sheng Long:** Supervision, Resources, Project administration, Funding acquisition. **Lan-Sun Zheng:** Supervision, Resources, Project administration, Funding acquisition. **Xiang-Jian Kong:** Writing – review & editing, Supervision, Software, Resources, Project administration, Methodology, Funding acquisition, Formal analysis, Data curation, Conceptualization.

Declaration of competing interest

The authors declare no competing interests.

Acknowledgements

This work was supported by the National Natural Science Foundation of China (Nos. 92461305, 92161203 and 92361301).

Appendix A. Supplementary data

Supplementary data to this article can be found online at https://doi.org/10.1016/j.cjsc.2025.100764.

References

[1] K.-P. Bai, C. Wu, J.-T. Lu, W.-P. Chen, M.-D. Cui, Y.-Z. Zheng, Assembling giant nanoclusters as heterogeneous catalysts for effectively converting CO_2 to CO under visible light, Small 21 (2025) 2412630.
[2] X. Yan, Z. Cai, C. Yi, W. Liu, M. Tan, Y. Tang, Anion-induced structures and luminescent properties of chiral lanthanide-organic frameworks assembled by an achiral tripodal ligand, Inorg. Chem. 50 (2011) 2346–2353.
[3] L. Wang, G. Fan, X. Xu, D. Chen, L. Wang, W. Shi, P. Cheng, Detection of polychlorinated benzenes (persistent organic pollutants) by a luminescent sensor based on a lanthanide metal-organic framework, J. Mater. Chem. A 5 (2017) 5541–5549.
[4] Q.-F. Xu, M.-T. Chen, M.-Y. Ye, B.-L. Liu, G.-L. Zhuang, L.-S. Long, L.-S. Zheng, Accurate prediction of the magnetic ordering temperature of ultralow-temperature magnetic refrigerants, ACS Appl. Mater. Interfaces 16 (2024) 32394–32401.
[5] Q.-F. Xu, M.-T. Chen, R.-T. Wu, L.-S. Long, L.-S. Zheng, Achieving magnetic refrigerants with large magnetic entropy changes and low magnetic ordering temperatures, J. Am. Chem. Soc. 146 (2024) 20116–20121.
[6] Q.-F. Xu, P. Zhao, M.-T. Chen, R.-T. Wu, W. Dai, L.-S. Long, L.-S. Zheng, Exceptional cooling capacity of $LiGd_{0.1}Yb_{0.9}F_4$ at sub-Kelvin temperatures, Adv. Mater. 37 (2025) 2414226.
[7] Y. Liu, J. Xiao, J. Koo, B. Yan, Chirality-driven topological electronic structure of DNA-like materials, Nat. Mater. 20 (2021) 638–644.
[8] S. Shaw, J.D. White, Asymmetric catalysis using chiral salen-metal complexes: recent advances, Chem. Rev. 119 (2019) 9381–9426.
[9] B. Han, X.-H. He, Y.-Q. Liu, G. He, C. Peng, J.-L. Li, Asymmetric organocatalysis: an enabling technology for medicinal chemistry, Chem. Soc. Rev. 50 (2021) 1522–1586.
[10] R. Sessoli, M.-E. Boulon, A. Caneschi, M. Mannini, L. Poggini, F. Wilhelm, A. Rogalev, Strong magneto-chiral dichroism in a paramagnetic molecular helix observed by hard X-rays, Nat. Phys. 11 (2015) 69–74.
[11] C.-Y. Li, L.C. Adi, K. Paillot, I. Breslavetz, L.-S. Long, L.-S. Zheng, G.L.J.A. Rikken, C. Train, X.-J. Kong, M. Atzori, Enhancement of magneto-chiral dichroism intensity by chemical design: the key role of magnetic-dipole allowed transitions, J. Am. Chem. Soc. 146 (2024) 16389–16393.
[12] M.S. Raju, K. Paillot, I. Breslavetz, G. Novitchi, G.L.J.A. Rikken, C. Train, M. Atzori, Optical readout of single-molecule magnets magnetic memories with unpolarized light, J. Am. Chem. Soc. 146 (2024) 23616–23624.
[13] L.-Z. Cai, Q.-S. Chen, C.-J. Zhang, P.-X. Li, M.-S. Wang, G.-C. Guo, Photochromism and photomagnetism of a 3d-4f hexacyanoferrate at room temperature, J. Am. Chem. Soc. 137 (2015) 10882–10885.
[14] R. Sessoli, Magnetic molecules back in the race, Nature 548 (2017) 400–401.
[15] J.A. Larrabee, W.R. Johnson, A.S. Volwiler, Magnetic circular dichroism study of a dicobalt(II) complex with mixed 5- and 6-coordination: a spectroscopic model for dicobalt(II) hydrolases, Inorg. Chem. 48 (2009) 8822–8829.
[16] R. Morassi, I. Bertini, L. Sacconi, Five-coordination in iron(II); cobalt(II) and nickel (II) complexes, Coord. Chem. Rev. 11 (1973) 343–402.
[17] J. Ferguson, D.L. Wood, K. Knox, Crystal-field spectra of d^3, d^7 ions. II. $KCoF_3$, $CoCl_2$, $CoBr_2$, and $CoWO_4$, J. Chem. Phys. 39 (1963) 881–889.
[18] I. Bertini, C. Mario, L. Sacconi, Polarized spectra of the trigonal bipyramidal $CoNP_3Br$ chromophore, J. Coord. Chem. 1 (1971) 73–74.
[19] I. Bertini, M. Ciampolini, D. Gatteschi, Single-crystal polarized electronic spectra of a CoN_5 chromophore, Inorg. Chem. 12 (1973) 693–696.
[20] J.A. Larrabee, C.M. Alessi, E.T. Asiedu, J.O. Cook, K.R. Hoerning, L.J. Klingler, G. S. Okin, S.G. Santee, T.L. Volkert, Magnetic circular dichroism spectroscopy as a probe of geometric and electronic structure of cobalt(II)-substituted proteins: ground-state zero-field splitting as a coordination number indicator, J. Am. Chem. Soc. 119 (1997) 4182–4196.
[21] M. Ciampolini, N. Nardi, Five-coordinated high-spin complexes of bivalent cobalt, nickel, and copper with tris(2-dimethylaminoethyl)amine, Inorg. Chem. 5 (1966) 41–44.
[22] J.P. Srivastava, Absorption spectrum of cobalt fluosilicate hexahydrate, J. Phys. Chem. Solid. 32 (1971) 279–283.
[23] X. Jia, T. Ge, S. Hou, S. Wang, Z. Wu, Y. Chi, J. Jin, Syntheses, structures and photophysical properties of Ni/Co–Ln coordination polymers, J. Mol. Struct. 1299 (2024) 137192.
[24] G.L.J.A. Rikken, E. Raupach, Pure and cascaded magnetochiral anisotropy in optical absorption, Phys. Rev. E 58 (1998) 5081–5084.
[25] G.L.J.A. Rikken, E. Raupach, V. Krstic, S. Roth, Magnetochiral anisotropy, Mol. Phys. 100 (2002) 1155–1160.
[26] C.-Y. Li, H. Xu, P.-M. Cheng, M.-H. Du, L.-S. Long, L.-S. Zheng, X.-J. Kong, From helices to crystals: multiscale representation of chirality in double-helix structures, J. Am. Chem. Soc. 145 (2023) 22176–22183.
[27] M. Aibibula, Y.-H. Song, H. Xu, M.-T. Chen, X.-J. Kong, L.-S. Long, L.-S. Zheng, Magneto-optical properties of chiral Co_2Ln and Co_3Ln_2 (Ln = Dy and Er) clusters, Inorg. Chem. 63 (2024) 8003–8007.
[28] V. Andrushchenko, D. Padula, E. Zhivotova, S. Yamamoto, P. Bouř, Magnetic circular dichroism of porphyrin lanthanide M^{3+} complexes, Chirality 26 (2014) 655–662.
[29] P.J. Stephens, Theory of magnetic circular dichroism, J. Chem. Phys. 52 (1970) 3489–3516.
[30] G.L.J.A. Rikken, E. Raupach, Enantioselective magnetochiral photochemistry, Nature 405 (2000) 932–935.
[31] T.N. Dais, R. Takano, T. Ishida, P.G. Plieger, Lanthanide induced variability in localised Co^{II} geometries of four triangular $L_3Co^{II}_3Ln^{III}$ complexes, RSC Adv. 12 (2022) 4828–4835.
[32] W.-P. Chen, P.-Q. Liao, P.-B. Jin, L. Zhang, B.-K. Ling, S.-C. Wang, Y.-T. Chan, X.-M. Chen, Y.-Z. Zheng, The gigantic $\{Ni_{36}Gd_{102}\}$ hexagon: a sulfate-templated "Star-of-David" for photocatalytic CO_2 reduction and magnetic cooling, J. Am. Chem. Soc. 142 (2020) 4663–4670.
[33] D. Schweinfurth, J. Krzystek, M. Atanasov, J. Klein, S. Hohloch, J. Telser, S. Demeshko, F. Meyer, F. Neese, B. Sarkar, Tuning magnetic anisotropy through ligand substitution in five-coordinate Co(II) complexes, Inorg. Chem. 56 (2017) 5253–5265.
[34] M. Ciampolini, Spectra of 3d five-coordinate complexes, Struct. Bond, Springer, 2008, pp. 52–93.
[35] B. Han, X. Gao, J. Lv, Z. Tang, Magnetic circular dichroism in nanomaterials: new opportunity in understanding and modulation of excitonic and plasmonic resonances, Adv. Mater. 32 (2020) 1801491.
[36] H. Ogasawara, A. Kotani, Calculation of magnetic circular dichroism of rare-earth elements, J. Phys. Soc. Jpn. 64 (1995) 1394–1401.
[37] J. Mack, M.J. Stillman, N. Kobayashi, Application of MCD spectroscopy to porphyrinoids, Coord. Chem. Rev. 251 (2007) 429–453.
[38] L. C. Adi, O.G. Willis, A. Gabbani, G.L.J.A. Rikken, L. Di Bari, C. Train, F. Pineider, F. Zinna, M. Atzori, Magneto-chiral dichroism of chiral lanthanide complexes in the context of Richardson's theory of optical activity, Angew. Chem. Int. Ed. 63 (2024) e202412521.
[39] N.F.M. Mukthar, N.D. Schley, G. Ung, Strong circularly polarized luminescence at 1550 nm from enantiopure molecular erbium complexes, J. Am. Chem. Soc. 144 (2022) 6148–6153.
[40] O.G. Willis, A. Pucci, E. Cavalli, F. Zinna, L. Di Bari, Intense 1400–1600 nm circularly polarised luminescence from homo- and heteroleptic chiral erbium complexes, J. Mater. Chem. C 11 (2023) 5290–5296.
[41] D.A. Gálico, J.S. Ovens, M. Murugesu, NIR-to-NIR emission on a water-soluble $\{Er_6\}$ and $\{Er_3Yb_3\}$ nanosized molecular wheel, Nanoscale 12 (2020) 11435–11439.
[42] N. Mavragani, D.A. Gálico, A.A. Kitos, M. Murugesu, Near-infrared magnetic circularly polarized luminescence and slow magnetic relaxation in a tetrazinyl-bridged erbium metallocene, J. Am. Chem. Soc. 147 (2025) 1387–1391.
[43] M. Pinsky, D. Avnir, Continuous symmetry measures. 5. The classical polyhedra, Inorg. Chem. 37 (1998) 5575–5582.
[44] K. Świątek, T. Surkova, A. Sienkiewicz, A. Zakrzewski, M. Godlewski, W. Giriat, Co^{2+} ions in ZnS_xSe_{1-x}:Co ESR and optical studies, Acta Phys. Pol. A 94 (1998) 593–596.
[45] S.M. Kaczmarek, G. Boulon, The presence of different oxidation states of cations in optical hosts on the base of $Co:SrLaGa_3O_7$, Opt. Mater. 24 (2003) 151–162.
[46] A.K. Mondal, T. Goswami, A. Misra, S. Konar, Probing the effects of ligand field and coordination geometry on magnetic anisotropy of pentacoordinate cobalt(II) single-ion magnets, Inorg. Chem. 56 (2017) 6870–6878.
[47] Z. Chen, L. Yin, X. Mi, S. Wang, F. Cao, Z. Wang, Y. Li, J. Lu, J. Dou, Field-induced slow magnetic relaxation of two 1-D compounds containing six-coordinated cobalt (II) ions: influence of the coordination geometry, Inorg. Chem. Front. 5 (2018) 2314–2320.
[48] S. Utsuno, T. Ando, M. Ishida, Chiroptical properties of five-coordinate complexes of nickel(II) and cobalt(II) containing an optically active ligand with nitrogen and phosphorus donor atoms, J. Coord. Chem. 38 (1996) 29–39.
[49] S. Ostrovsky, Z. Tomkowicz, W. Haase, High-spin Co(II) in monomeric and exchange coupled oligomeric structures: magnetic and magnetic circular dichroism investigations, Coord. Chem. Rev. 253 (2009) 2363–2375.
[50] J.A. Larrabee, G. Schenk, N. Mitić, M.J. Riley, Use of magnetic circular dichroism to study dinuclear metallohydrolases and the corresponding biomimetics, Eur. Biophys. J. 44 (2015) 393–415.